Characterization and understanding of mechanical variability of elastomer: application in automotive valve testing in low cycles fatigue

Rodolphe Forasacco, Marie-Pierre Deffarges, Florian Lacroix, Florent Chalon, Stéphane Couarraze, Mathieu Venin, Stéphane Méo

Mechanics & Industry **25**, 14 (2024)

https://doi.org/10.1051/meca/2024007

Mechanics & Industry

Available online at:
www.mechanics-industry.org

REGULAR ARTICLE

OPEN ACCESS

Characterization and understanding of mechanical variability of elastomer: application in automotive valve testing in low cycles fatigue

Rodolphe Forasacco[1,2,*], Marie-Pierre Deffarges[1], Florian Lacroix[1], Florent Chalon[1], Stéphane Couarraze[2], Mathieu Venin[1], and Stéphane Méo[1]

[1] Laboratoire de Mécanique Gabriel Lamé, Université de Tours, INSA CVL, Université d'Orléans, 29 rue des Martyrs, 37300, Joué les Tours, France
[2] Continental Automotive Toulouse, 1 Av. Paul Ourliac, 31100, Toulouse, France

Received: 21 August 2023 / Accepted: 12 February 2024

Abstract. Currently, rubber automotive valves are appropriate for passenger vehicles that operate at speeds lower than 210 km/h. However, beyond this threshold, the mechanical stress imposed on the elastomer is far more intense, increasing the risk of cracks caused by the cyclic accelerations and decelerations of the vehicle. This work delves into valve damage at high speed to gain insights into the factors contributing to failures. Fractographic analysis on valves has facilitated a thorough comprehension of valve damage by precisely pinpointing the location of crack initiation and its propagation within the volume of the elastomer. Nevertheless, the correlation between failures and valve durability is not straightforward, primarily due to variations in bench test equipment. Therefore, in order to eliminate the influence of bench test equipment-related variations, a fatigue campaign was conducted on laboratory specimens. This aimed to exclusively characterize the variability in rubber fatigue. Additionally, to achieve a higher level of representativeness of valve application, Hencky's invariants were employed to establish an equivalent kinematic mechanical valve state on these specimens. Experimental results attest an intrinsic variability of the rubber material. Subsequently, a fractography study on these specimens has provided a clearer insight into the primary material weaknesses, specifically focusing on the agglomeration of black carbon. A microstructural analysis using scanning electron microscopy (SEM) was performed to assess the batch dispersion state in correlation with specimen durability.

Keywords: Elastomer / Tire valve / Variability / Fatigue / Structure / Fractography / Hencky's invariants

1 Introduction

In the automotive sector, tyres are sealed by contact with the rim and an inflation valve that runs through it. Depending on the maximum speeds reached by the vehicles, automotive valves can be made of rubber or metal. Rubber valves are less mechanically resistant and are intended for passenger cars that do not exceed about 210 km h^{-1} while metal valves are designed for faster cars. Although the valves and tire provide a seal between the rim and the outside environment, tire pressure may decrease slightly over time depending on the ride. Underinflated tires affect road holding, increase the risk of puncture or bursting, and are responsible for wasting billions of liters of fuel each year. In order to address these issues, legislation associated with safety standards requires the integration of TPMS (Tire Pressure Monitoring System) in cars for car manufacturers.

There are two types of TPMS, the one with an indirect measurement that uses a calculation with ABS (Anti-lock Braking System) or ESP (Electronic Stability Program) and the one with a direct measurement via a sensor positioned inside the tire and fixed most often to the back of the valve (Fig. 1). TPMS with direct measurement give the transverse acceleration, temperature, and air pressure in each wheel. This information is transmitted to the driver on the dashboard via an electronic module (low radio frequencies) integrated into the TPMS housing associated with a central receiver located in the vehicle.

Rubber valves are used for cars with common performance and are not designed for high-speed application where mechanical stresses are much greater. In such cases, the stress induced by the rotation of the wheel exposes the rubber to a risk of failure which can lead to

* e-mail: rodolphe.forasacco@etu.univ-tours.fr

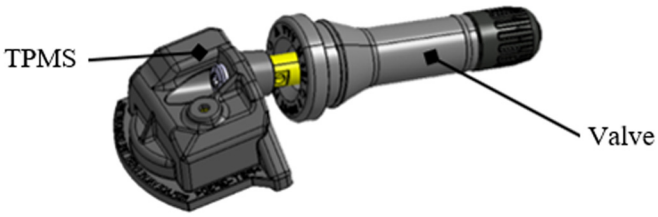

Fig. 1. Assembly of valve and TPMS.

cracking of the elastomer as shown in Figure 2 and cause a loss of total tire pressure. In order to determine the critical speed limit of the rubber valve, the characterization of the valve fatigue shall be carried out on a specific test bench described in Section 3.2. These tests aim to reproduce driving cycles to judge dynamic performance. It appears that the results indicate a significant dispersion of valve durability. Some valves have early cracks of about four hundred cycles leading to a loss of tightness while the others remain operational after a long time of test fatigue (more than twenty thousand cycles). Continental has identified that the significant dispersion of valve durability is partly related to equipment and test means. For this study, attention is focused on the intrinsic behavior of the elastomer. In this case, the present work aims to determine whether the rubber material also induces variability in dynamic performance. To be representative of valve application, an original approach is developed to exclusively characterize rubber variability on laboratory samples through an experimental fatigue campaign. The peculiarity of these experiments is that the kinematic mechanical state of the sample is close to that of the valves. To establish the kinematic mechanical state, Hencky invariants introduced by Criscione et al. [1] were used. The study focus on examining failure mechanism of the rubber valve under high-speed application and laboratory sample. Additionally, the structural aspect of the rubber was analyzed to identify the main source of failure.

2 State of the art

2.1 Rubber and black carbon

Elastomers are highly sought materials in the industrial world, particularly due to their incompressible hyperelastic behavior, damping property, thermal resistance to both low and high temperatures, as well as their sealing ability for air and fluids. They are used in almost every activity sectors (automotive, medical industry, aerospace, construction, etc.). They are complex materials, composed of numerous ingredients of different natures (rubber gums, fillers, oils, additives, vulcanization systems, etc.) each playing an important role in the acquisition of specific properties. Fillers are fundamental ingredients in elastomers, they are used to provide mechanical reinforcement. They are rigid elements that increase stiffness and provide good resistance to fatigue. The most reinforcing and commonly fillers used in the industry are carbon blacks, as in the rubber valve. They offer the best compromise in terms of mechanical properties (tensile strength and elongation) and they have good compatibility with the chemical structure of rubbers. Carbon black fillers are agglomerated spherical particles, they adopt two types of structure: primary and secondary ones. Primary structures are clusters of elementary particles known as aggregates (Fig.. 3). Depending on the carbon black type, these aggregates can be composed of a few tens (low structure) to a few hundred (high structure) of particles. The aggregate is the smallest dispersible element within the elastomer matrix. Secondary structures are assembled of aggregates known as agglomerates. Agglomerates are linked by low-energy bonds [3] (Van der Waals, π, Hydrogen, etc.) which can be broken during the mixing process [4,5]. In this way, an agglomerate can split into several aggregates of low and/or high structure. According to ASTM D1765 classification (Tab. 1), carbon blacks are categorized into different grades based on size and structure. Particle diameters can range from a few nanometers to approximately 500 nm. The most reinforcing fillers are those with small particle diameters with high specific surface.

2.2 Fatigue

The study of fatigue behavior in elastomers is divided into two approaches: crack initiation and crack propagation. In most cases, fatigue cracks initiate from heterogeneities mostly related to the elastomer ingredients (fillers, metal oxides, etc.) but also from inner weakness (pollutions, voids, and cavities). These stress concentration are privileged sites for crack initiation. According to literature, Saintier et al. [7] demonstrated that carbon black agglomerates of approximately 100 µm diameter are responsible for crack initiation in natural rubber elastomer. Masquelier [8] identified initiation sites of different natures into natural rubber, mainly zinc oxides and carbon black agglomerates. Other authors such as Grandcoin et al. [9] also showed that crack initiation occurs around an agglomerate site. Knowing that they studied silicone material, initiation takes place around a silica agglomerate. In elastomers, crack initiation is not always caused by an intrinsic defect located in the elastomer matrix; it can also be related to the geometry of the part/specimen or to joint surface. Hainsworth et al. [10] illustrated that crack initiation takes place within a high-stress concentration zone located at the upper edge of the sample while Poisson and al. [11] documented crack initiation occurring on a diabolo-shaped specimen at the joint surface. Cavities possibly created during mechanical loading also contribute to crack initiation. Le Cam et al. [12] demonstrated that cracks start from ZnO particles due to decohesion with the elastomer matrix. Weng et al. [13] highlighted the decohesion of ZnS particles leading to crack initiation. They also showed that shortly after initiation, these decohesions evolve into larger cavities, causing the coalescence of multiple initiations until specimen failure.

Either on surface or into the rubber matrix, chronologically, the crack initiation leads to its propagation, causing the failure of the specimen or a part of it. After examining fracture surfaces of silicones and carbon black-filled natural rubber subjected to fatigue, Hainsworth [10] decomposed the fracture surfaces into three distinct regions. The author demonstrated that the first region is associated with crack

Fig. 2. Defective and operational valves after fatigue characterization.

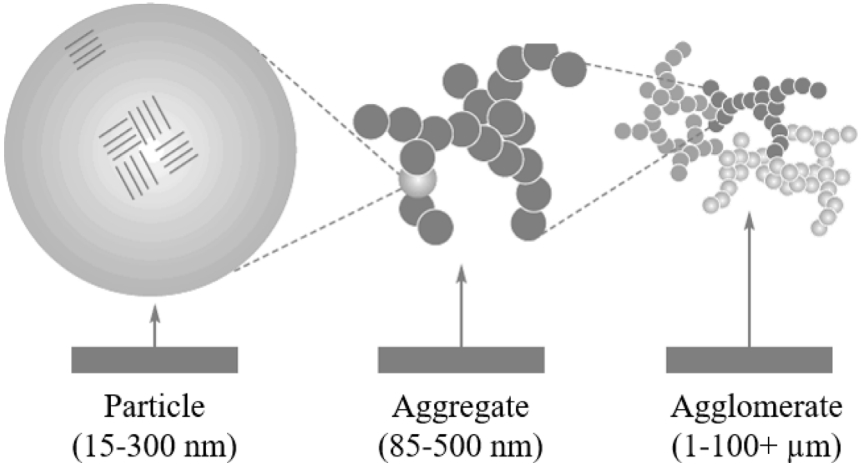

Fig. 3. Carbon black agglomerate scheme [3].

Table 1. ASTM D1765 carbon black classification [6].

Name	Standard abbreviation	ASTM designation	Particle size (nm)	Avg. N_2 surface area (m^2/g)
Super abrasion furnace	SAF	N110	15–18	124–130
Intermediate SAF	ISAF	N220	20–25	112–115
High abrasion furnace	HAF	N330	28–36	76–80
Fast extrusion furnace	FEF	N550	39–55	39–41
General purpose furnace	GPF	N660	56–70	34–36
Semi reinforcing furnace	SRF	N770	71–96	31–32
Fine thermal	FT	N880	180–200	17–20
Medium thermal	MT	N990	250–350	7–9

initiation. Successively, the second zone is attributed to a phase of rapid propagation, and finally, the last one represents the final rupture by tearing. Le Cam et al. [12] presented the propagation mechanisms in carbon black-filled natural rubber. They showed that as the crack size increases, ellipsoidal zones with ligaments forms around the decohesions. These micro cracks widen in conjunction with the primary crack, revealing new cavities that propagate perpendicularly to the propagation direction. The quantity and size of microcracks increase, destroying ellipsoidal zones, which provoke a failure of the crack tip and lead to the growth of the main crack. Afterward, the propagation process is repeated. Hainsworth [10] observed a similar propagation process to Le Cam et al. study, they also found ligaments in cracks without ellipsoidal shape. Saintier et al. [7] discussed the aspect of stress-induced crystallization and its influence on the crack propagation direction in natural rubber. They found that when crystallization occurs, an anisotropic behavior is established at the crack tip, causing bifurcation of the latter in

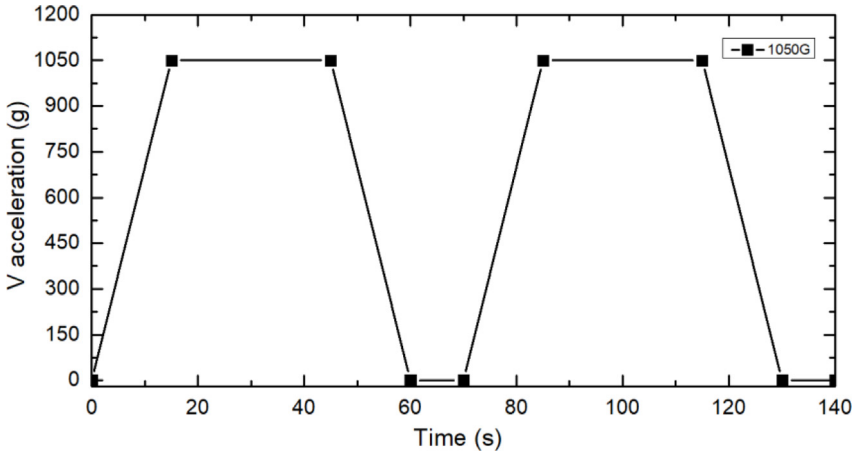

Fig. 4. SpinTest acceleration profile at 1050 g.

multiple directions simultaneously. In the absence of crystallization and under relaxation conditions, no deviation is observed, and the main crack naturally propagates perpendicular to the loading direction. Although the crack propagation pattern depends on the type of elastomer, it also varies depending on the type of loading. Ayoub et al. [14] noted that the featured surfaces are different under tension, torsion, and compression loadings.

As described previously, it has been shown by various authors that initiation can originate from a defect and then propagate through the material. In this context, these bibliographic studies can contribute to the understanding of valve damage to identify rupture causes.

3 Material and methods

3.1 Material

Rubber valve is composed of chloroprene gum filled with high reinforced carbon black, oil, protector agents, and metal oxide crosslinking system combined with accelerators. Valves and rubber specimens have been acquired from the same masterbatch and are molded in the same molding conditions of temperature and time. Specimens are taken from a rubber sheet of 2 mm thickness.

3.2 SpinTest equipment

The durability of the valves in fatigue has been characterized on specific test machine called SpinTest. For a single test, it is possible to independently test 18 valves with their own air cavity and unique rim hole definitions under specific driving conditions. Throughout the test, the sensors communicate through RF (Radio Frequency) antenna positioned inside the bench test. It is then possible to retrieve the pressure history of the 18 cavities along with their associated sensors, which gives valve failure cycle corresponding to an instantaneous pressure loss. SpinTest characterization enables to assess the dynamical performance of valves and estimates their service life. To carry out the test, firstly, valves are inserted through their attributed rim hole. TPMS sensor are screwed to valves. Afterwards, the whole is positioned on a specific 17-inches wheel attached to a rotating shaft. Then, temperature and mechanical profiles are selected by the test operator and the shaft is set in rotation.

In the automotive field, this rotational speed is expressed by the induced centrifugal acceleration which is normalized by the acceleration (gravitational constant g) see equation given below (1). This acceleration is conventionally called V.

$$V = \frac{r\omega^2}{g}, \tag{1}$$

where, r is the distance between the wheel center and the gravity center of TPMS and valve, ω is the speed rotation, and g the acceleration of gravity.

In this study, rubber valves are characterized by trapezoidal mechanical profile at 265 km h^{-1} which is equivalent to 2136 rpm and an acceleration V of 1050 g, see Figure 4. The wheel is set in rotation at 2136 rpm in 15 s with a linear acceleration of 142.4 m s^{-2}. This rotational speed is maintained for 30 s, followed by a deceleration over 15 s until the wheel stops. Finally, a pause time of 10 s is marked before starting a new cycle. Tests are carried out at 50 °C.

To evaluate the durability of the 18 valves tested simultaneously in the SpinTest, a performance index I_{perf} is introduced, corresponding to a number between 0 and 1 to quantify the dynamical performance of each batch productions. It is estimated that from 10,000 cycles onwards, the valve has met its performance requirements. For example, at 1050 g, 10,000 cycles correspond to a mileage of 33,125 km at 265 km h^{-1}. A performance index of 1 indicates excellent dynamic performance with no failure before reaching 10 000 cycles for all 18 valves. If valve failure occurs before 10 000 cycles, the index is calculated by recovering the failure cycle of each valve. The formula is

Table 2. Performance index of studied batches.

Batch name	Performance index
A	0.26
B	0.59
C	0.82

as follows:

$$I_{\text{perf}} = \frac{1}{18}n + \frac{1}{18}\sum_{m=1}^{m=18}\frac{CyRupt_m}{CyPerf}. \quad (2)$$

In equation (2), *CyPerf* determine the number of cycles equivalent to a good dynamical performance, here set at 10,000, n is the number of operational valves after *CyPerf*, m the number of defective valves below *CyPerf*, and *CyPerf* correspond to the rupture cycle number.

In this study, three rubber batches have been analyzed. SpinTest performance index of those batches are indicated in Table 2.

3.3 Fatigue equipment

Fatigue tests on specimens were carried out on fatigue testing machine Instron 8872 using 1 kN cell (class 0.5). Specific rubber specimens of 2 mm thickness are subjected to uniaxial tension and are mounted on a multi-station device capable of testing five specimens simultaneously. Identification of specimen failure is based on decrease of the storage modulus *E*' measured by the equipment. Tests are conducted at a constant deformation rate of 1 mm s^{-1} to eliminate viscosity effects. Finally, tests are performed at 50 °C as for the SpinTest characterizations. The experimental protocol is detailed in Section 4.5.

3.4 Microscopic and structural analysis

Featured surfaces of valve and specimen have been observed by Scanning Electronic Microscopy Field Emission Gun (SEM-FEG JSM 7200F) at Continental laboratory in Toulouse. Samples were metallized with a sediment gold/paladium.

Internal structure of the rubber material was examined by Transmission Electronic Microscopy (JEM-1400 JEOL) at the University of Angers (SCIAM). The micrographs are acquired with a GATAN Orius 832 camera. The electron source is a tungsten filament, and the acceleration voltage used is 120 kV. In this study, a rubber cube is extracted from the valve. It is then placed on a support in a sucrose droplet before being introduced into cryogenic chamber of the ultramicrotome (LEICA Cryo-ultramicrotome UC7-FC7). The temperature is controlled using liquid nitrogen within a range of −80 °C to −90 °C. Thin slices of rubber were obtained using a diatom diamond knife at a cutting speed of 1 mm s^{-1} at (–90 °C). The thickness of the cuts is approximately 500 nm. Cuts are subsequently collected in a new sucrose droplet and deposited onto grids at room temperature. The grids are then rinsed to remove traces of sucrose before being observed with a TEM (Fig. 5).

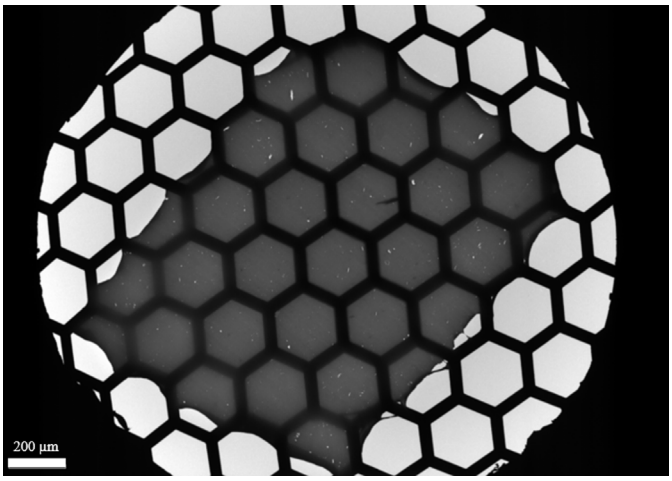

Fig. 5. Copper grid with thin rubber cut for transmission electron microscopy (TEM) analysis.

Rubber structure have been investigated by PHOENIX V|TOME|X S240 micro CT-scan at Continental laboratory in Toulouse using 0.7 µm nanofocal tube.

3.5 Numerical calculation

Ogden second order hyperelastic law have been used for rubber modeling on ABAQUS at 50 °C. Five mechanical tests were performed: biaxial and uniaxial tension, uniaxial compression, volumetric compression and pure shearing to model the mechanical behavior.

The modeling is constructed following the actual phases of the product assembly. Firstly, an insertion phase occurs where the valve is introduced into the rim hole. It is then followed by a phase called “recoil” 1where the valve repositions itself in the sealing area after insertion. It involves the material properties related to cyclic relaxation characterization tests. Afterwards, an equilibrium phase is established through relaxation. And finally, a virtual wheel is set in rotation, causing centrifugal forces (volumetric forces) on the elastomer until reaching an acceleration of 1050 g.

4 Results and discussion

4.1 Valve damaging

Depending on the characteristics of the valve (weight distribution, size, shape) and the design of the TPMS, the center of gravity is located either inside the wheel or outside the wheel. Therefore, when the rotation speed increases, the valve and its sensor are subject to a pendulum effect. In this study, the configuration of the valve and the sensor used results in a lift down configuration which means that

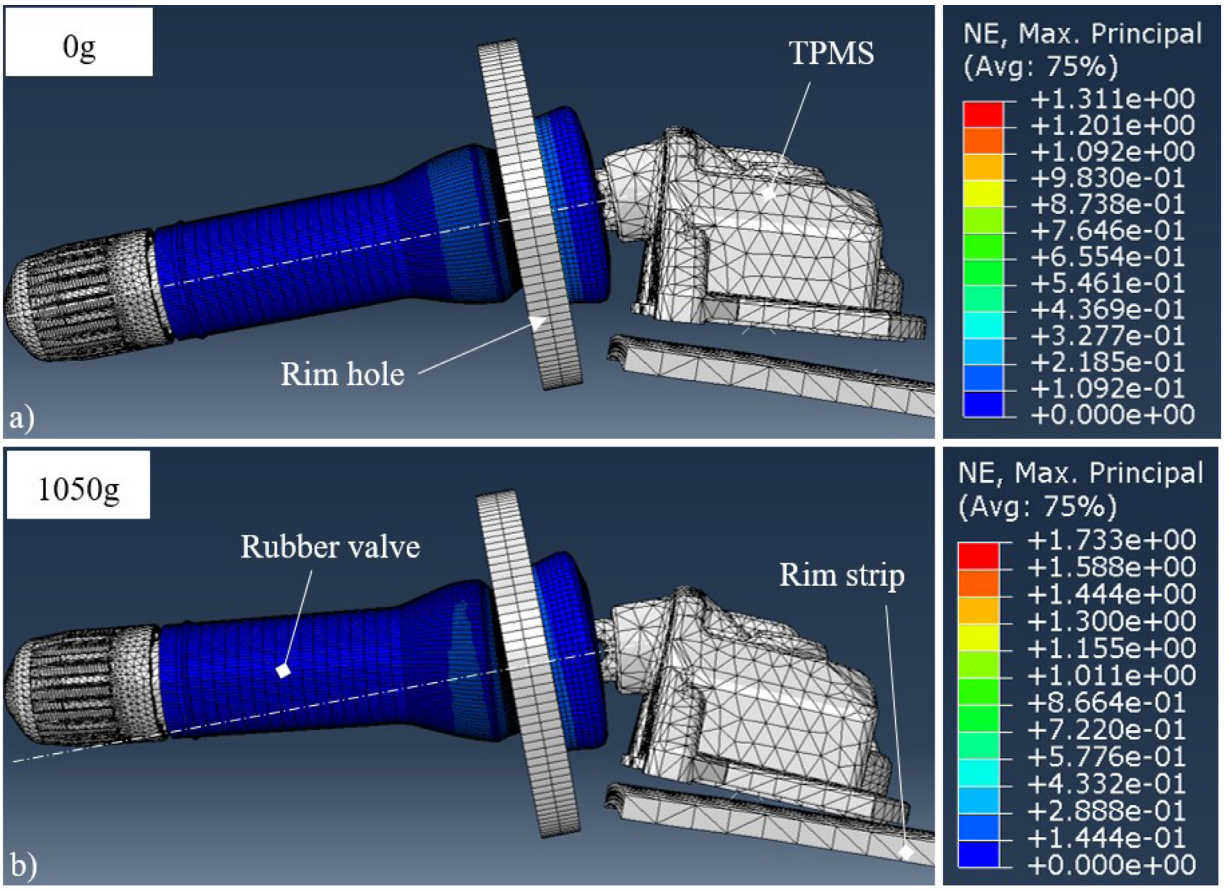

Fig. 6. Modeling of nominal elongation distribution of the rubber valve. (a) No rotational motion applied, 0 g; (b) rotational motion of a wheel at an acceleration of 1050 g.

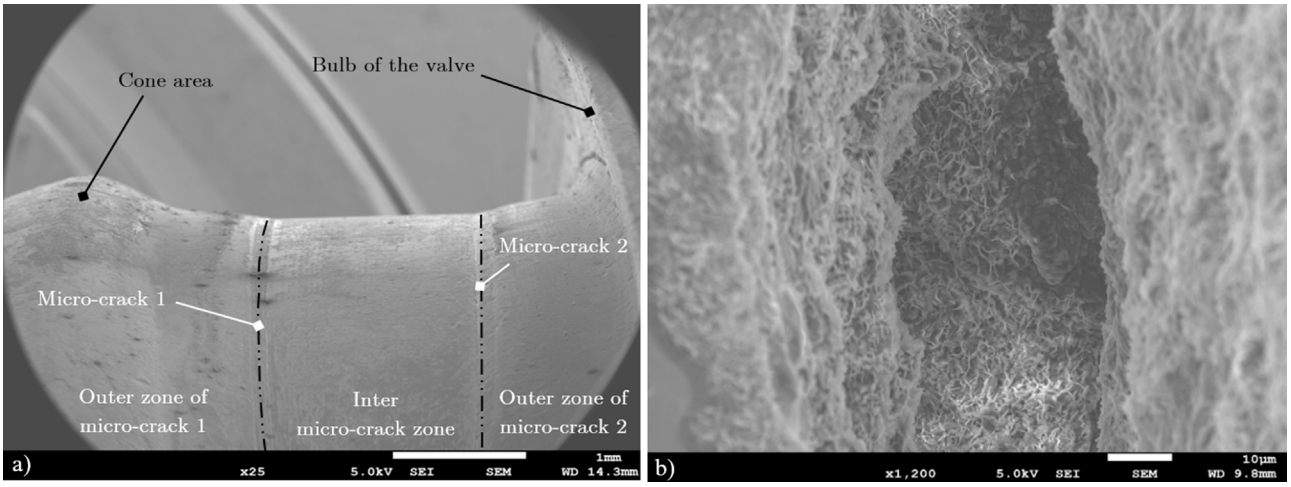

Fig. 7. SEM images on operational valve after SpinTest characterization at 1050 g. (a) Sealing area observation; (b) optical magnification of the micro-crack 1.

the valve will lift until the TPMS comes into contact with the rim bottom strip. Numerical model in Figure 6. illustrates these statements.

Consequently, stress concentration on rubber is located at the contact with the outer edge of the chamfer of the rim hole. Induced by centrifugal force, this stress may lead to crack initiation. SEM analysis on operational valves after SpinTest have confirmed it. Indeed, valves still assuring the tightness indicate a facture initiation at the surface as shown in Figures 7a and 7b. The initiation location is also confirmed through the presence of striations on the featured surfaces of defective valves (Figs. 8 and 9),

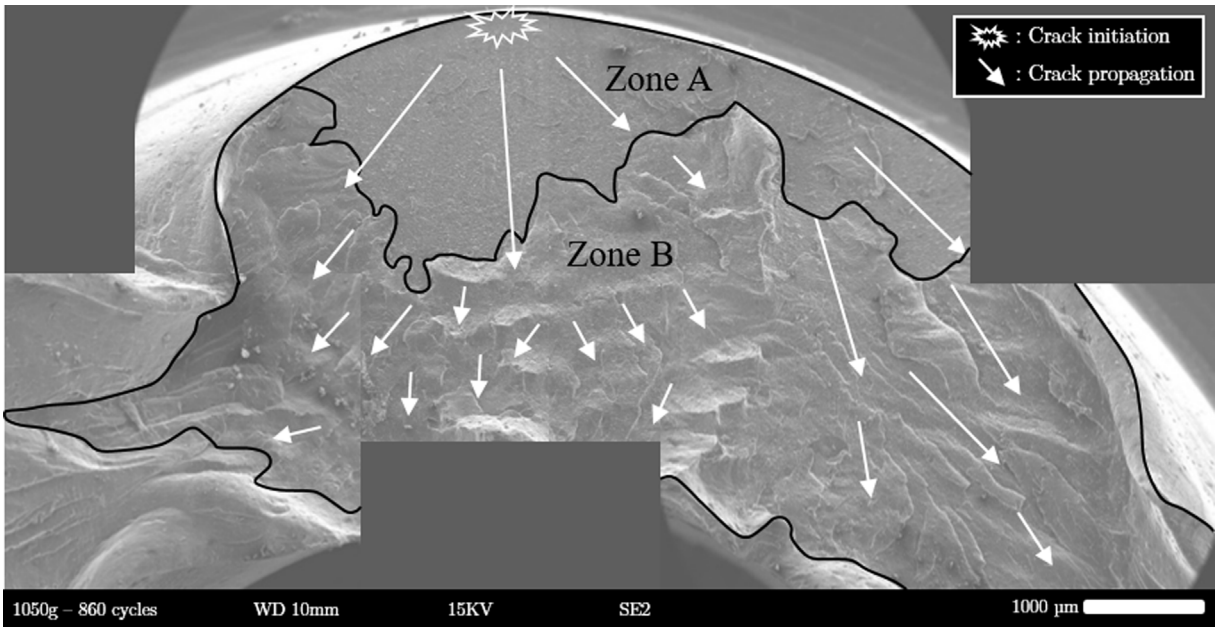

Fig. 8. SEM reconstruction images of featured crack surface after SpinTest characterization at 1050 g. Zone A: unidirectional propagation crack; Zone B: multi directional propagation crack.

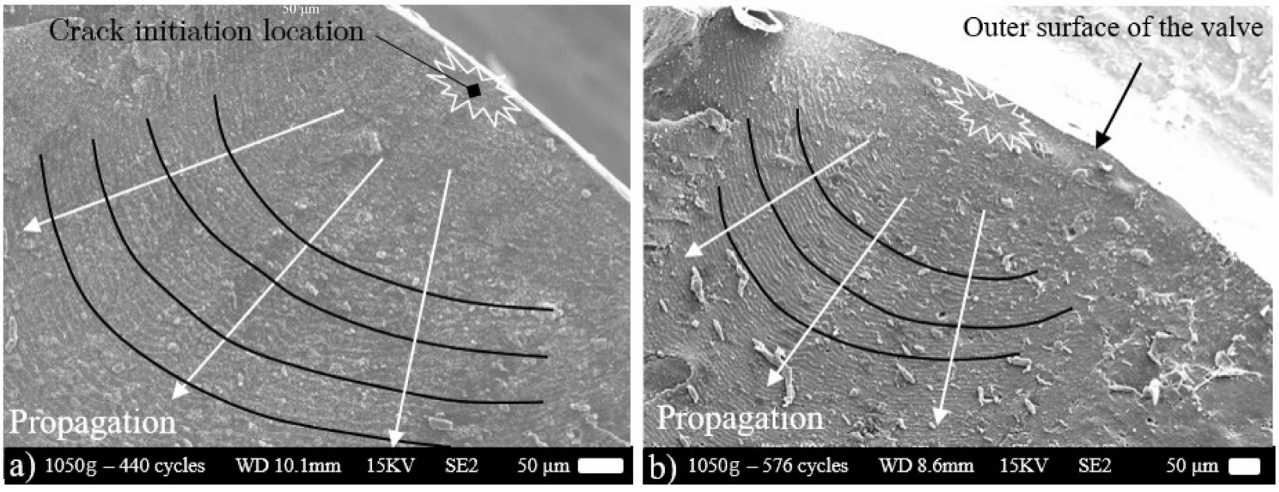

Fig. 9. SEM images of featured surface at the outer surface in the initiation area.

providing qualitative information about the crack propagation direction as well as the crack growth rates. By ascending, the very first striations can be observed near the outer surface of the valve. This is the first stage where the crack begins to form (Region A). It is characterized by slow and stable propagation of the crack, with closely spaced inter-striation distances (a few microns apart). Local stresses are high, resulting in localized deformation and progressive crack growth. At a certain stage, the crack deviates from its initial path due to the presence of stresses, discontinuities, or inclusions in the material (Region B). This is manifested by changes in the streak orientation (Fig. 10). Based on the inter-striation distances in this new region (approximately 20–30 µm), propagation accelerate, leading to higher propagation speeds compared to the slow crack growth phase.

Microscopic analysis gives a good understanding of the chronology of cracks propagation, but it does not reveal neither the causes of failure nor if the material exhibits variability. In order to characterize intrinsic elastomer variability, an experimental fatigue campaign guided by numerical simulation (calculation of Hencky tensor invariants) is conducted on custom-shaped test specimens. This will help to identify the weak areas of the material more accurately through fractography. The Hencky tensor and its invariants are presented in the next section.

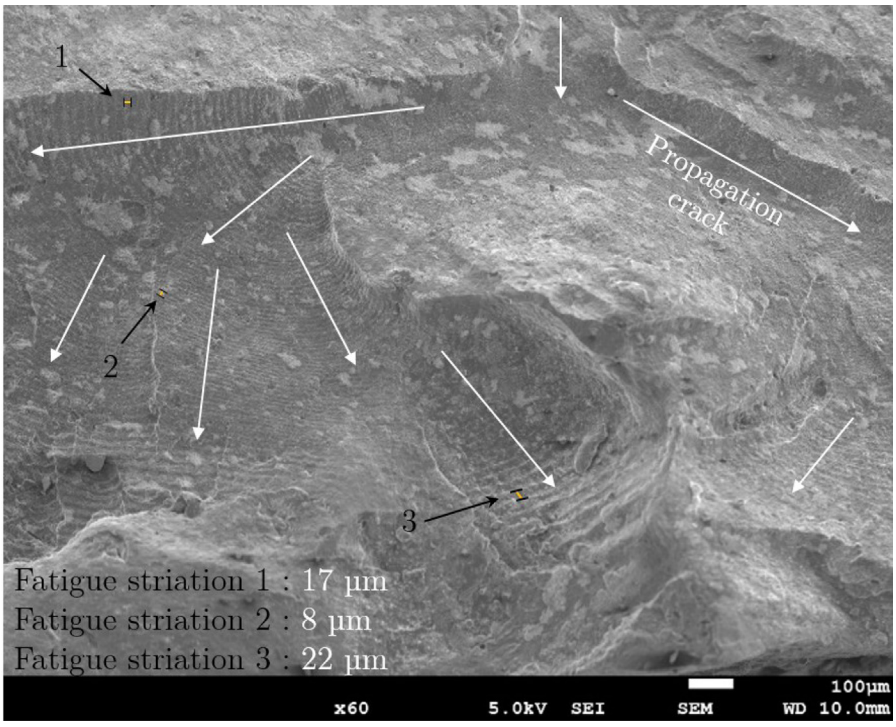

Fig. 10. SEM image of featured surface in the propagation phase.

4.2 Hencky tensor and invariants

The deformation gradient $\overline{\overline{F}}$ is a mathematical representation used to describe the deformation or distortion undergone by a material when subjected to mechanical loading or other external forces. It can be decomposed into a pure deformation followed by a rotation, denoted as $\overline{\overline{R}}$, or vice versa (through a unique polar decomposition):

$$\overline{\overline{F}} = \overline{\overline{R}}\,\overline{\overline{U}} = \overline{\overline{V}}\,\overline{\overline{R}}. \tag{3}$$

The tensors $\overline{\overline{U}}$ and $\overline{\overline{V}}$ represent, respectively, the right pure deformation tensor associated with the initial configuration and the left pure deformation tensor associated with the final configuration. As for $\overline{\overline{R}}$, it represents the rotations and is orthogonal ($\overline{\overline{R}}^{T} = \overline{\overline{R}}^{-1}$).

Figure 11 illustrates the two described decompositions. We will add that the determinant of $\overline{\overline{F}}$ is called the Jacobian and will be denoted, J.

These deformation tensors can also be expressed in the following form:

$$\overline{\overline{U}} = \sqrt{\overline{\overline{F}}^{T}\,\overline{\overline{F}}} \text{ and } \overline{\overline{V}} = \sqrt{\overline{\overline{F}}^{T}\,\overline{\overline{F}}}. \tag{4}$$

By squaring these tensors, we define the right Cauchy-Green deformation tensor, denoted $\overline{\overline{C}}$ in the Lagrangian configuration, and $\overline{\overline{B}}$ the left Cauchy-Green tensor in the Eulerian configuration.

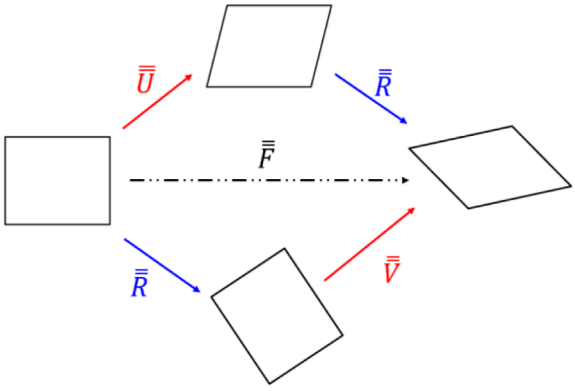

Fig. 11. Polar decomposition of the deformation gradient $\boldsymbol{F}$.

$$\overline{\overline{U}}^{2} = \overline{\overline{F}}^{T}\,\overline{\overline{F}} = \overline{\overline{C}}, \tag{5}$$

$$\overline{\overline{V}}^{2} = \overline{\overline{F}}\,\overline{\overline{F}}^{T} = B. \tag{6}$$

From these tensors, Seth-Hill (1968, 1978) define strain measures to quantify the stretch. In the Eulerian configuration, they are expressed as equation (7). At order 0, $\boldsymbol{A}_{=0}$ also known as the logarithmic strain tensor,

corresponds to the Hencky strain tensor $\overline{\overline{\boldsymbol{H}}} = \ln \overline{\overline{\boldsymbol{V}}}$.

$$A_m = \begin{cases} \frac{1}{m}\left(\overline{\overline{V}}^{m} - \overline{\overline{I}}\right), \forall\, m \neq 0 \\ \ln \overline{\overline{V}} \text{ if } m = 0. \end{cases} \quad (7)$$

It is worth noting that the Hencky strain tensor can be decomposed into a deviatoric part, $\overline{\overline{\boldsymbol{H}}}^{D}$ associated with distortion, and a spherical part, $\overline{\overline{\boldsymbol{H}}}^{S}$ which refers to volumetric deformations. These terms will be used to explain the calculation of invariants in the following section.

$$\overline{\overline{H}} = \overline{\overline{H}}^{D} + \overline{\overline{H}}^{S}, \quad (8)$$

$$\overline{\overline{H}}S = \frac{1}{3} tr\left(\overline{\overline{H}}\right)\overline{\overline{I}}, \quad (9)$$

$$\overline{\overline{H}}^{D} = \overline{\overline{H}} - \frac{1}{3} tr\left(\overline{H}\right). \quad (10)$$

$\overline{\overline{\boldsymbol{H}}}^{S}$ Notably, in the case of incompressible materials: $= 0$.

As introduced in the general overview, certain hyperelastic models describe the energy density $\boldsymbol{W}$ based on the invariants In of $\overline{\overline{\boldsymbol{C}}}$ (or $\overline{\overline{\boldsymbol{B}}}$) or the principal stretches λ_n of $\overline{\overline{\boldsymbol{V}}}$. However, these models have the particularity of being effective and accurate only within a certain range of deformations. Beyond this range, they exhibit significant errors in predicting the mechanical behavior. In order to contribute to the improvement of these models, Criscione et al. [1] introduce three new invariants K_1,K_2 and K_3 obtained from the Hencky tensor. These invariants have the advantage of providing physical meanings to the state of deformation of the deformed material. Invariant K_1 refers to volumetric deformations, and is a number defined between -∞ and +∞ where 0 corresponds to an isochoric transformation. K_2 represents the intensity of deformation distortion and is a positive or zero number. Lastly, K_3 indicates the mode of loading and is contained within the interval [–1 ; 1].

– K_3 =1 corresponds to a uniaxial tension case.

– K_3 = 0 represents a pure shear case.

– K_3 = - 1 is equivalent to a uniaxial compression case.

These invariants are expressed by the following relations:

$$K_1 = tr\left(\overline{\overline{H}}\right), \quad (11)$$

$$K_2 = \sqrt{\overline{\overline{H}}^{D}} : \overline{\overline{H}}\, D, \quad (12)$$

$$K_3 = \frac{3\sqrt{6}}{K_2^3} det\left(\overline{\overline{H}}^{D}\right), \quad (13)$$

where, $\overline{\overline{\mathrm{H}}}^{D}$ corresponds to the deviatoric part of $\overline{\overline{\boldsymbol{H}}}$.

Assuming the material is incompressible, the volume is preserved, and the transformation is isochoric, which means $\boldsymbol{J} = det\boldsymbol{F} = 1$. By identification:

$$K_1 = tr\left(\ln \overline{\overline{I}}\right) = 0, \quad (14)$$

$\overline{\overline{\boldsymbol{H}}}^{S}$ becomes zero. The expressions for K_2 and K_3 are then simplified and can be expressed solely in terms of their deviatoric component, where $\lambda^{V}_{1,2,3}$ are the eigenvalues of $\overline{\overline{\boldsymbol{V}}}$.

$$K_2 = \sqrt{\overline{\overline{H}} : \overline{\overline{H}}} = \sqrt{\left(\ln \lambda_1^V\right)^2 + \left(\ln \lambda_2^V\right)^2 + \left(\ln \lambda_3^V\right)^2}, \quad (15)$$

$$K_3 = \frac{3\sqrt{6}}{K_2^3} det\left(\overline{\overline{H}}\right) = \frac{3\sqrt{6}}{\left(\sqrt{\left(\ln\lambda_1^V\right)^2 + \left(\ln\lambda_2^V\right)^2 + \left(\ln\lambda_3^V\right)^2}\right)^3} \ln \lambda_1^V \ln \lambda_2^V \ln \lambda_3^V. \quad (16)$$

In the context of the study, it is proposed to use these invariants to identify the "deformation state" of the crack initiation zone on the valve. For convenience, they will be used assuming the material is incompressible.

4.3 Valve deformation state with Hencky's invariants

Obtained from modeling, Figures 12 and 13 respectively depict the distribution of K_2 and K_3 under a loading equivalent to 1050 g. From K_2 distribution, it can be observed (indicated by the red area) that the sealing area is highly exposed to deformation, as well as the outer surface with the two circular marks. These areas are associated to the contact with the rim hole and correspond to the initiation position of the crack. Blue areas represent regions with low mechanical strain. Regarding K_3, the analysis of invariants only has physical significance for elements that have non-zero values of K_2. The overall analysis of the elements with K_2 greater than 1 reveal that approximately 57% of the elements are subjected to mixed loading of tension and shear ($K_3\varepsilon$[0;1]) , while 43% are subjected to loading combining compression and shear ($K_3\varepsilon$ [-1 ; 0]). As an indicative observation, the invariants suggest that tensile and shear deformations are predominant in the overall analysis of the sealing area.

As described previously, whether the valve is defective or operational, it has been demonstrated that crack initiation on valves is localized on the surface and can lead to propagation within the volume in certain cases.

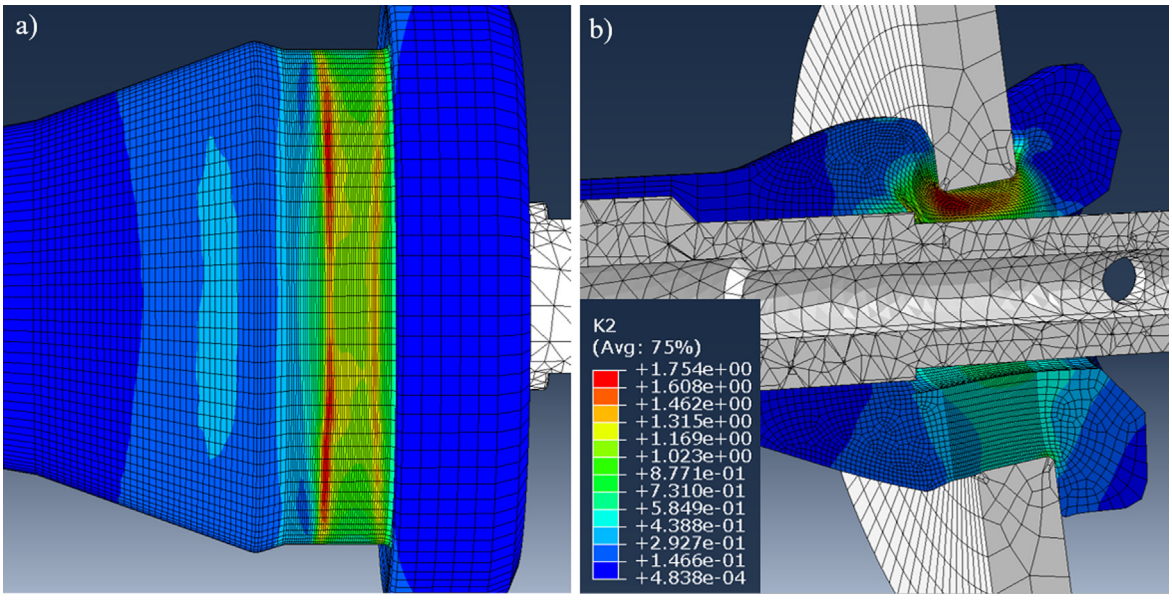

Fig. 12. K_2 representation of the valve at 1050 g − Centrifugal force is applied along z-axis; (a) undeformed view; (b) cross-sectional view.

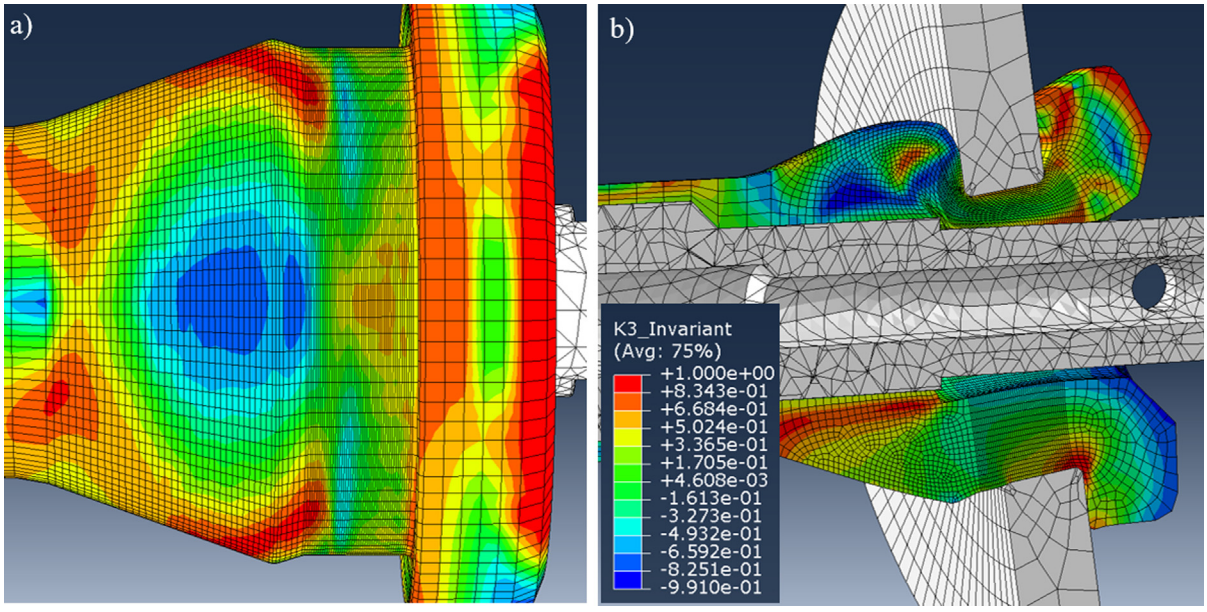

Fig. 13. K_3 representation of the valve at 1050 g − Centrifugal force is applied along z-axis; (a) Undeformed view; (b) cross-sectional view.

Consequently, it was decided to analyze the invariants at the nodes of the 6 central elements on the crack initiation. The values of the invariants K_2 and K_3 corresponding to the crack initiation zone are displayed in Table 3. The intervals defining the minimum and maximum values of the invariants will be considered. The results indicate that the state deformation at the crack initiation is a combination of shear and tension ($K_3 > 0$).

Although the characterization of the invariants is important at 1050 g, it is also the case at 0 g. Indeed, a load ratio R_{K2}, calculated Table 3, between 0 g and 1050 g can be established. Its usefulness will be revealed in the experiment campaign part. This ratio has been computed using the average values of K_2.

4.4 Customized specimen representative of deformation valve state via Hencky's invariants

The second step of the approach, based on the established deformation state of the valve using Hencky's invariants, is to design a representative specimen of the valve's loading condition through simulation using ABAQUS.

Table 3. Hencky's invariants value on crack initiation location of the valve at 1050 g and 0 g.

Hencky's invariants	K_2 (0 g)	K_2 (1050 g)	K_3 (1050 g)
Minimum	0.61	1.21	0.46
Maximum	0.83	1.41	0.67
Overall	0.73	1.32	0.53
Standard deviation	0.06	0.05	0.05
Ratio: $R_{K_2} = (K_2(0G)/K_2(1050G)$	0.55		

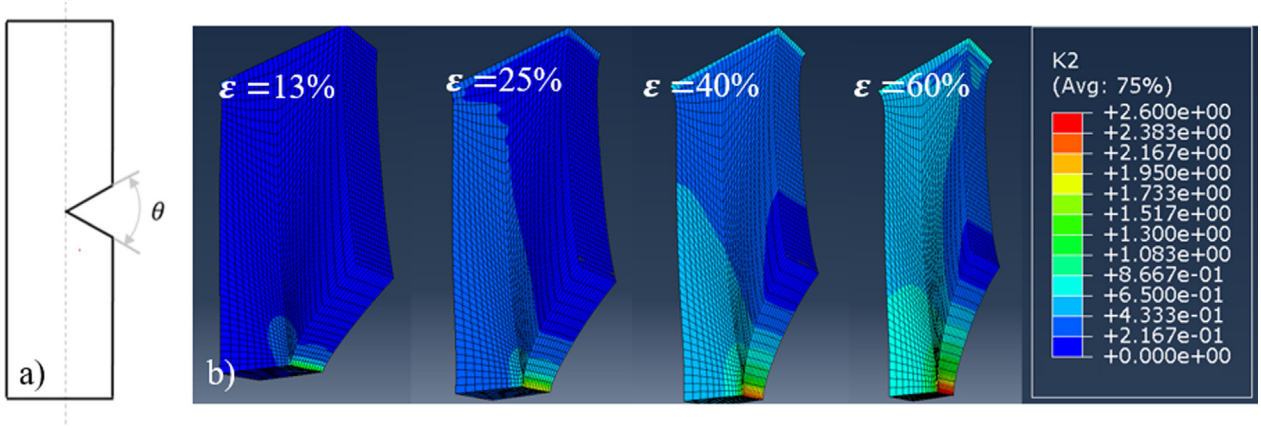

Fig. 14. (a) Schematic representation of the design of the specimen. $L0 = 20$ mm; (b) K_2 representation at several amplitude displacements – ε denotes the global deformation.

The objective is to create a sample geometry in which the invariants at the crack initiation closely match those obtained from the valve. The authors point out that the aim is not expressly to reproduce the loading (in terms of both stress and strain) seen by the material when it is loaded, but to characterize its variability by using a state of deformation on a test specimen close to that involved in the valve. This proposal involves designing a customized geometry with a controlled crack initiation location. For this purpose, as crack initiation on valve occurs on the outer rubber surface and then propagates, the fatigue approach adopted is conducted on notched specimens.

The first step consists in determining a geometry where the loading condition, driven by the invariant K_3, is comparable to that obtained on the valve. The invariants on the specimen must necessarily fall within the boundary values of the valve deformation state K_3. Subsequently, the utilization of K_2 will help determine the deformation intensity equivalent to 1050 g.

Without describing all the tested geometries, it turns out that the satisfactory correspondence to the K_3 invariants is achieved with a notched specimen at mid-width with a 60° angle (Fig. 14a). We will limit the discussion to the selected geometry. The identification of the best candidate was based on the results of the invariants calculated to the singularity on the edge in the plane of symmetry. Figure 14b highlights the intensity of deformation and clearly demonstrates that the deformation concentration occurs at this edge.

Just like in valve analysis, a nodal calculation was considered for the specimen. K_2 and K_3 are calculated when the specimen is under tension at several levels of deformation. Figures 15 and 16 respectively display the values of K_3 and K_2 for the nodes along the geometric singularity within the thickness of the specimen. Here, four levels of overall deformation on this graph are chosen (13%, 25%, 40%, and 60%). The intervals of the invariants on the valves previously determined at 1050 g are also represented to better visualize the area of interest. Results reveal a symmetry plane in the median plane of the specimen's thickness (Figs. 15 and 16).

Focusing first on the K_3 invariants, it can be observed that regardless of the overall nominal deformation, the invariants are not constant along the thickness of the specimen. For 13% nominal deformation ($\varepsilon = 0.13$), as the elements move away from the median axis, the values of the invariants increase, indicating that the nodes are more exposed to a tensile load compared to the central element. It can also be noted that the values at the edges of the specimen are outside the interval that defines the state of deformation on valve. Also, as the deformation rate increases (25%, 40%, 60%), the representations of K_3 differ. By comparing the invariants at the median axis, it can be observed that as the deformation amplitude increases, the value of the invariants also increases. However, the values at the edges of the specimen do not follow the same trends. In fact, these values decrease significantly and fall outside the interval on the valves for

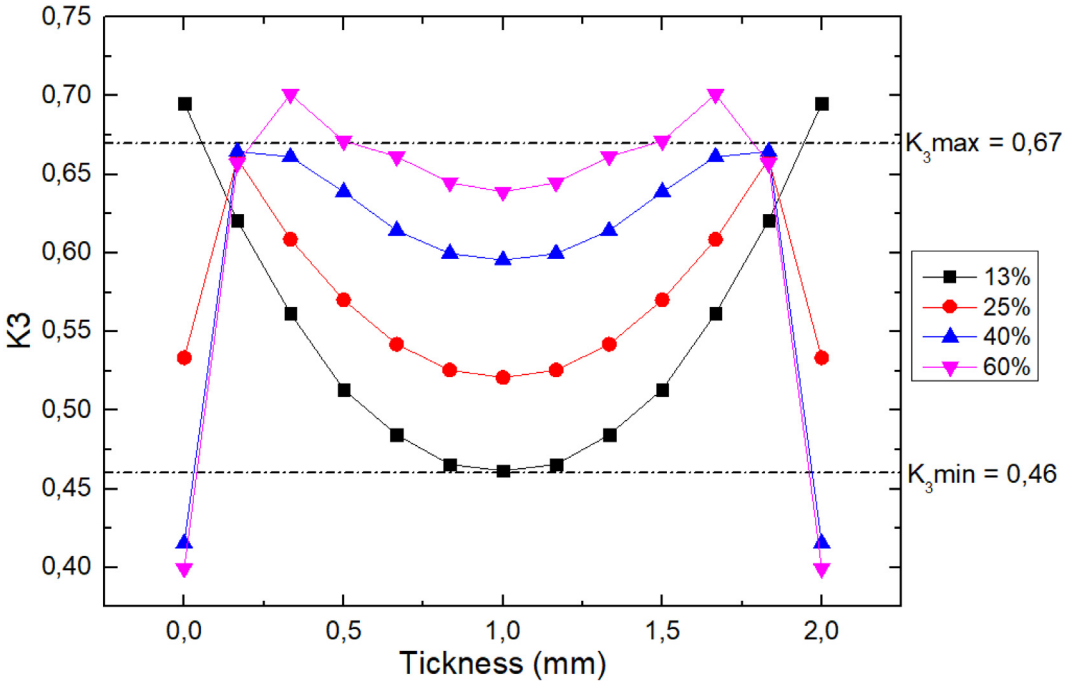

Fig. 15. Influence of the strain on invariants K_2 values on the singularity of the customized specimen.

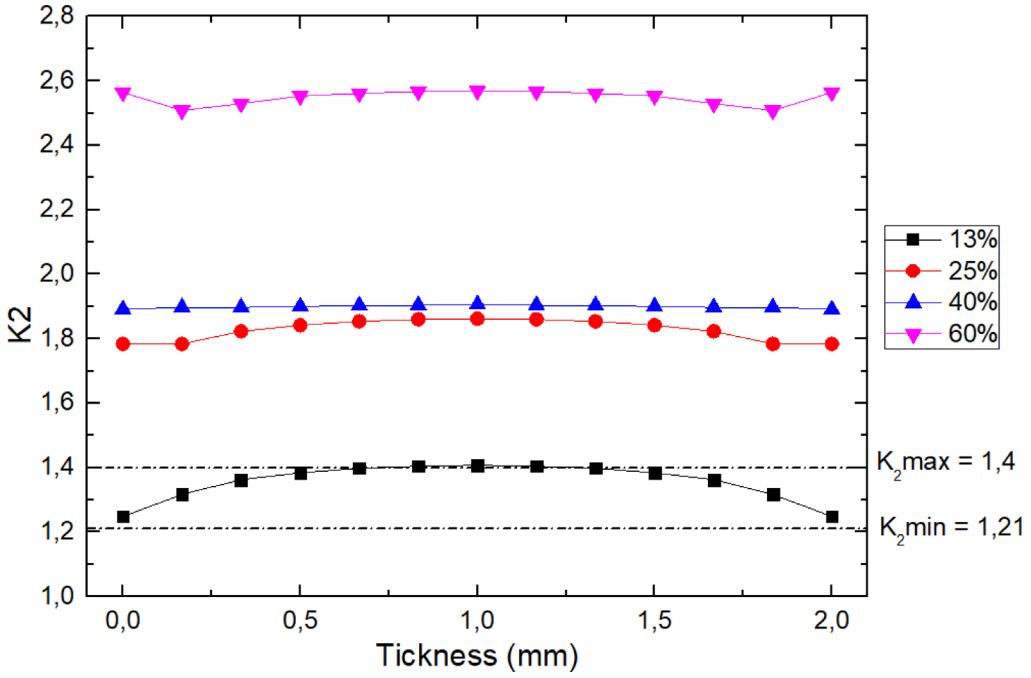

Fig. 16. Influence of the strain on invariants K_2 values on the singularity of the customized specimen.

40% and 60% deformation (Fig. 15). These differences can be attributed to edge effects. Nevertheless, 88% of the elements remain within the interval, which is still acceptable. In Figures 16, the correlation with the K_2 invariants shows that a global deformation of 13% perfectly matches the established state of deformation on the valves at 1050 g. It can be observed that the values only fluctuate slightly for the same nominal deformation level. However, for deformation rates higher than 13%, a considerable increase in K_2 is observed, taking it outside the targeted interval.

The analysis of invariants using the Hencky tensor shows a satisfactory correlation for the notched specimen at 60° subjected to 13% overall nominal deformation. This configuration theoretically replicates a deformation state comparable to the one obtained on valves under loading of 1050 g.

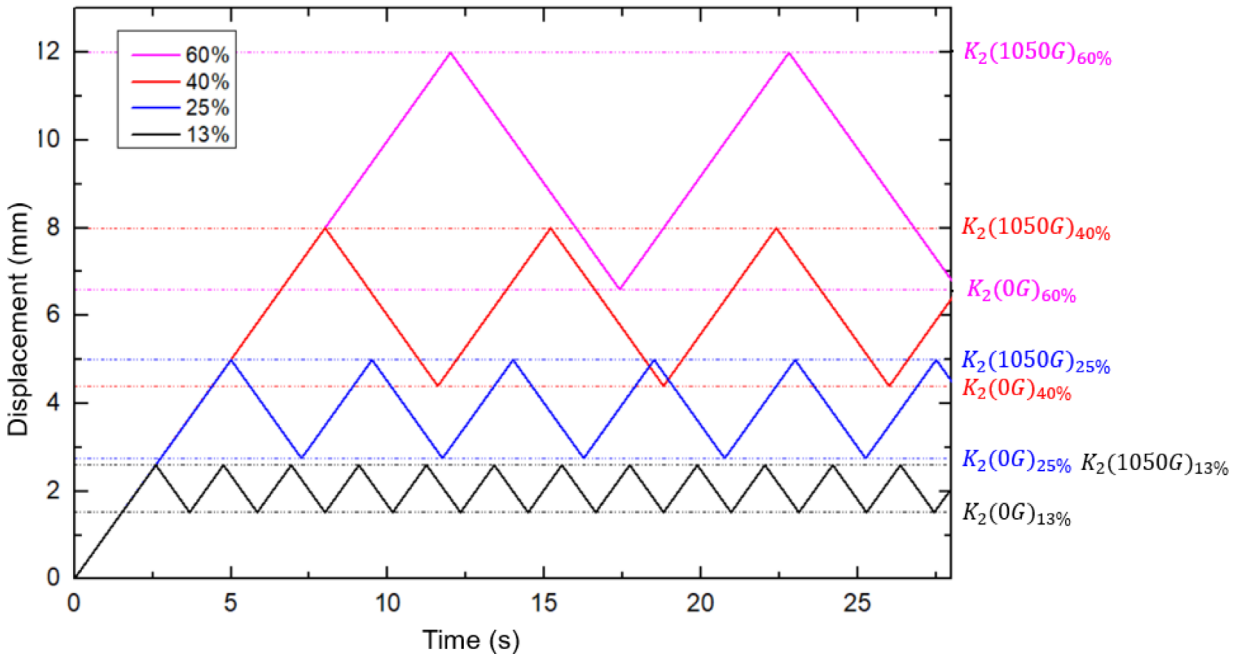

Fig. 17. Fatigue mechanical profiles selected.

4.5 Experimental fatigue campaign

Previously, a representative geometry of the deformation valve state subjected to an equivalent centrifugal acceleration of 1050 g using the K_3 invariant has been established. Numerical modeling on this geometry also allows determining the nominal global deformation to be applied in order to position the sample in a state of distortion (K_2) close to that obtained on the valve. Now, the intrinsic variability of the material in fatigue can be characterized under loadings similar to those "truly" experienced by the material in the initiation zone on part. These recent results establish an equivalence between the state on the valve and that obtained on the specimen for 13% tension deformation. Knowing that the objective is to highlight any mechanical variability, other nominal global deformations have been explored as well (25%, 40%, and 60%).

As for SpinTest, batches A, B and C will be characterized. Regarding the experimental protocol, specimens are subjected to triangular loading controlled by displacement at different amplitudes, as shown in Figure 17. The load ratio R_{K2} between K_2 (0 g) and K_2 (1050 g), obtained through the modeling on the valve allows to determine the minimum displacement amplitude of the triangular signals. Following experimentation at 13% global deformation, tests revealed excessively long experimentation durations. Consequently, only the other amplitudes were characterized for convenience. Fatigue results are displayed in Table 4 and Figure 18.

As expected, specimen's lifespan mostly depends on maximum global amplitude. Regardless of the displacement amplitude, significant differences between batches are observed. It seems that valve batches with good dynamical performance have also good fatigue durability on specimens and vice versa. There is a direct correlation between specimen lifetimes and the performance index I_{perf} (SpinTest) as shown in Table 4.

However, performance variability is noticeable. Although batch A has the lowest lifetimes, it exhibits low dispersion compared to batches B and C. This is demonstrated by the $R_{\text{max/min}}$ ratio (Tab. 4), which represents the ratio between the number of cycles to failure of the specimen with the longest lifetime and the one with the shortest. For batch A, this ratio is less than 2 regardless of the applied strain rate, while for batches B and C, it is significantly higher. At the 60%-33% amplitude, due to the occurrence of early failures, these ratios are 14.7 and 32.1 for B and C, respectively, which demonstrate that rubber exhibits an intrinsic variability. At lower amplitudes, the $R_{\text{max/min}}$ ratios are considerably reduced. These early failures, characteristic of prompt damage, could be explained by the encounter of significant singularities along the crack path. In order to gain further insights into these disparities, a fractographic and structural analysis have been carried out.

4.6 Featured specimen surface and structural aspect

4.6.1 Fractography

The crack initiates at the singular edge until it propagates into the volume. The first failed specimens show unique fractures where crack propagation deviates from its natural direction due to encountering a singularity along the crack path. SEM observations presented below were conducted on these specimens.

Without revealing the presence of significant defects or directional striations in the crack tips, microscopic observations highlight a differentiation of chemical contrasts on the fracture surfaces (Fig.19a). Although some

Table 4. Fatigue results.

Batch name	Number of cycles at break		
	$\varepsilon = 60\% - 33\%$	$\varepsilon = 40\% - 22\%$	$\varepsilon = 25\% - 13\%$
	11,100	16,600	31,400
Batch A	11,900	22,300	34,500
$I_{perf} = 0.26$	15,200	24,300	34,500
	18,100	24,760	35,200
	/	26,400	41,100
$R_{max/min}$	1.6	1.6	1.3
Average batch A	$14\,075 \pm 3\,217$	$22\,872 \pm 3\,799$	$35\,340 \pm 3\,540$
	$\varepsilon = 60\% - 33\%$	$\varepsilon = 40\% - 22\%$	$\varepsilon = 25\% - 13\%$
	1800	15,900	36,500
Batch B	5600	26,500	48,400
$I_{perf} = 0.59$	21,100	18,700	129,700
	22,200	26,600	181,900
	26,600	51,200	208,800
$R_{max/min}$	14.8	3.2	5.7
Average batch B	$15\,460 \pm 11\,013$	$30\,750 \pm 14\,127$	$121\,060 \pm 77\,305$
	$\varepsilon = 60\% - 33\%$	$\varepsilon = 40\% - 22\%$	$\varepsilon = 25\% - 13\%$
	5340	44,300	84,100
Batch C	16,100	138,900	98,200
$I_{perf} = 0.82$	80,800	156,900	116,000
	101,000	+325,500	126,300
	171,700	+325,500	208,700
$R_{max/min}$	32.1	7.3	2.5
Average batch C	$74\,988 \pm 67\,791$	$198\,220 \pm 123\,812$	$126\,660 \pm 48\,646$

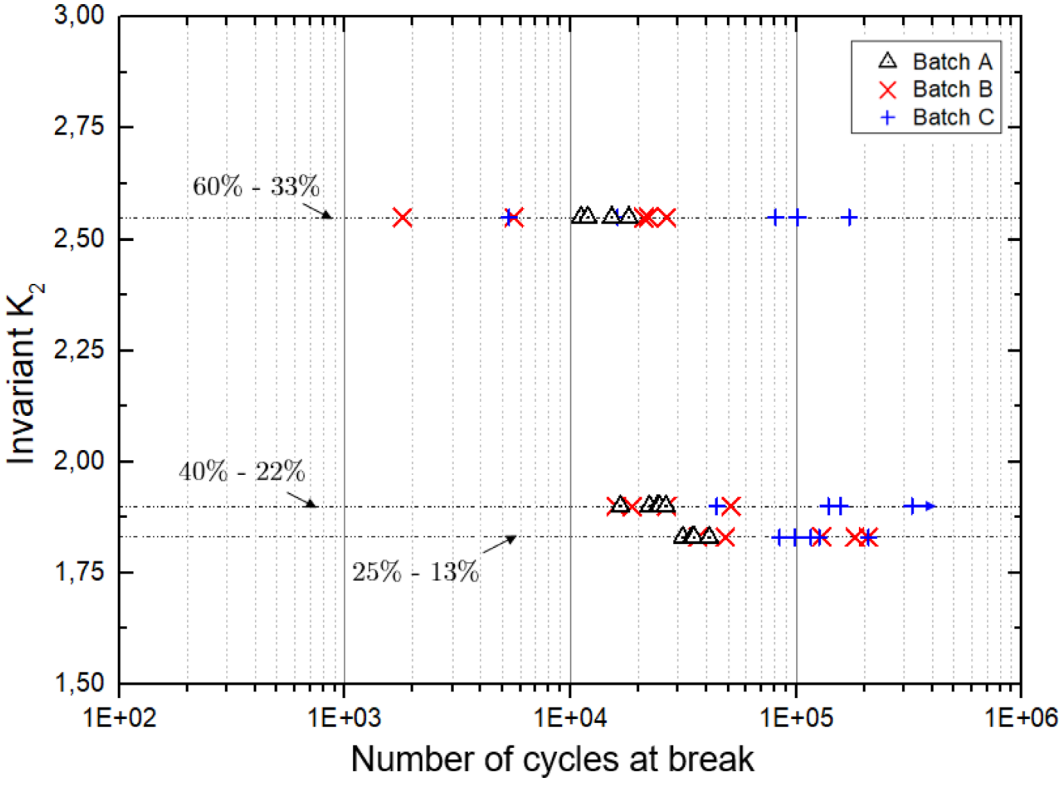

Fig. 18. S-N plots for different rubber batches.

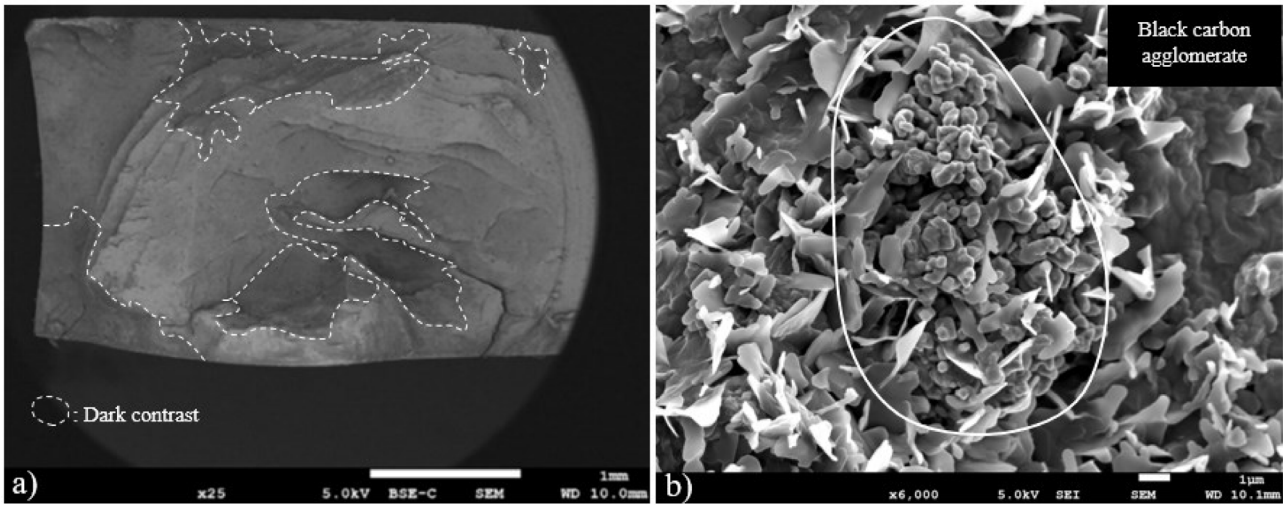

Fig. 19. SEM images of the fracture surfaces of specimens. (a) Backscattered electron of the featured surface; (b) secondary electron of a black carbon agglomerate surrounded by tongues.

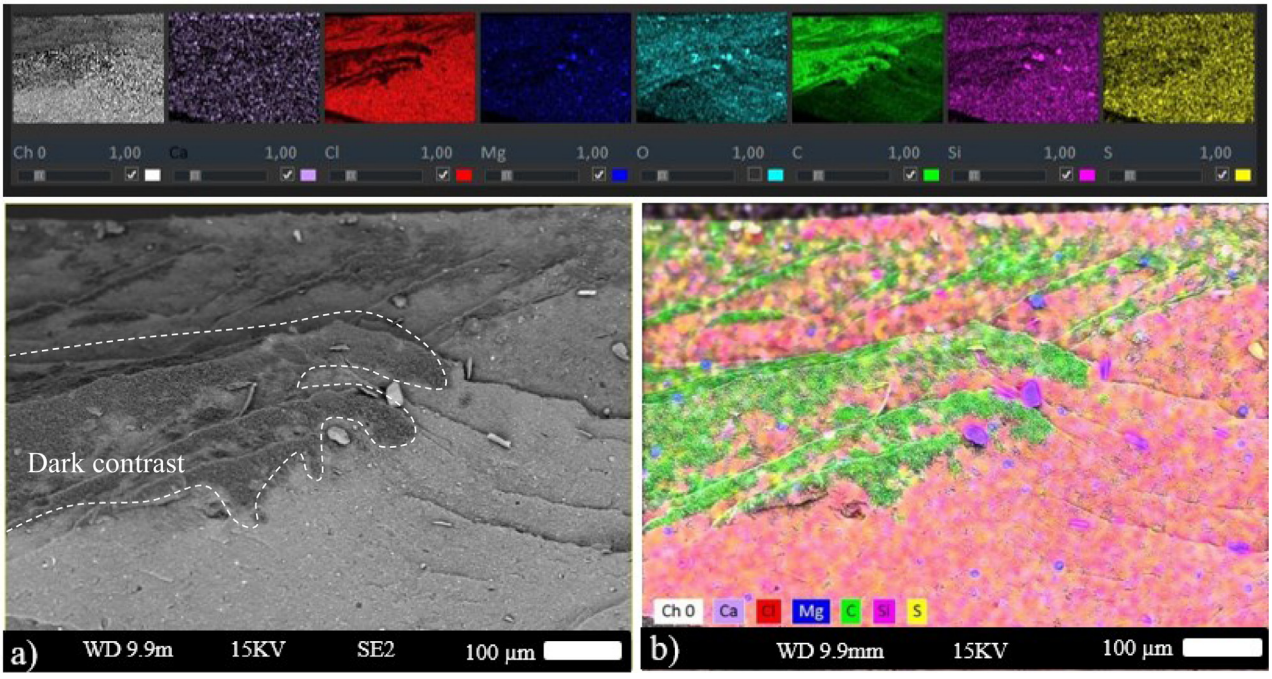

Fig. 20. (a) SEM images on featured surface of specimen; (b) EDX mapping of dark contrast.

areas may be obscured due to topography, the associated mappings on these darker surfaces (Fig. 20.) reveal concentrations of carbon. The absence of chlorine indicates that these contrasts could be, a priori, associated with carbon black. Those aspects are observed on all specimen and their surface can extend over several hundred microns. At higher magnification (Fig. 19b), dark contrasts exposed a specific surface morphology called tongue which is symptomatic in chloroprene rubber of fatigue damage and thermo-oxidation. Previously studied in the literature for fatigue loading on chloroprene rubber (CR) and natural rubber (NR), Legorju-Jago [15] was the first to observe these structures. She associated them with fatigue damage combined with a thermo-oxidation phenomenon. Through an experimental fatigue campaign under immersion in water and then under nitrogen, the author demonstrated that in the absence of oxygen, the fracture surfaces do not exhibit these morphologies. Therefore, the presence of these structures is likely generated by the combination of cyclic loading, induced self-heating, and the presence of oxygen.

On Figure 19b, one carbon black aggregate is also noticeable and is surrounded by those tongues. The particle diameters of the spotted aggregate, ranging from 200 to

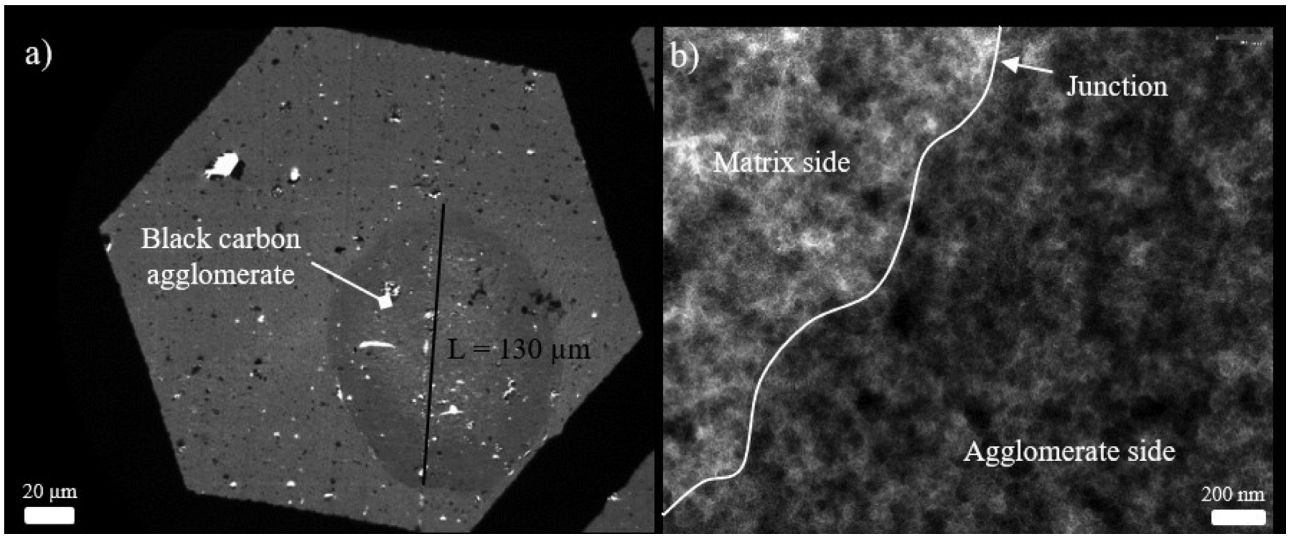

Fig. 21. (a) Frame containing a black carbon agglomerate; (b) TEM image of the junction of elastomere matrix and black carbon agglomerate.

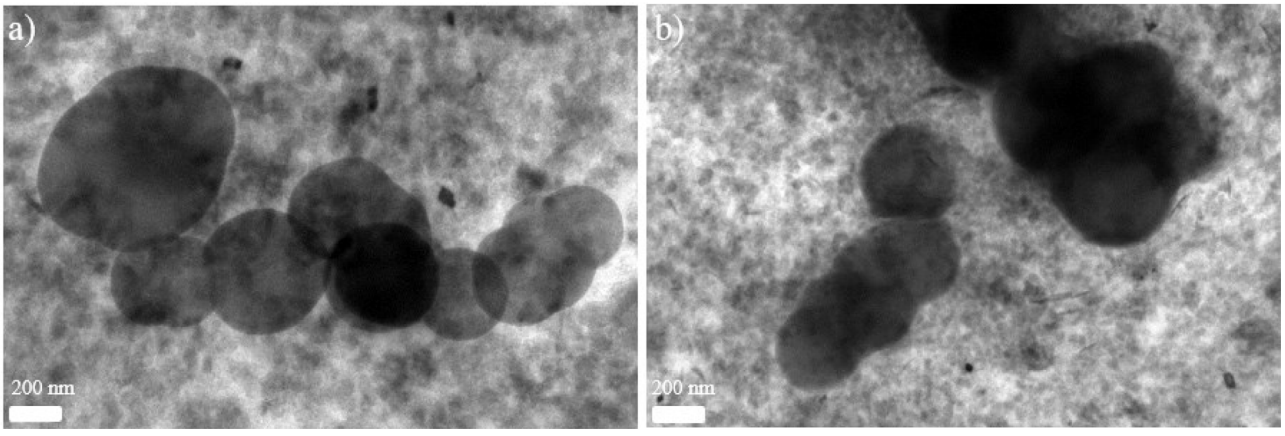

Fig. 22. SEM images of carbon black pollution.

350 nm, indicates that this element does not correspond to the high reinforced carbon black of rubber valve formulation. Thus, it corresponds to a pollution which may ease the crack propagation. Given the extensive surface area covered by carbon on the fracture surfaces, firsts specimen failures may result from poor dispersion and/or poor distribution of carbon black particles. Microstructural analyses of the elastomer presented subsequently will allow quantifying black carbon dispersion state and correlation with index performance batches.

4.6.2 TEM observations

The grayscale contrast is reversed compared to SEM, thus the heavier the element, the darker it appears. Conversely, the elements appearing bright correspond to low volumetric density elements. In this section, only black carbon agglomerates are analyzed. They are identified by the gray ellipsoidal elements as illustrated in Figure 21aa. At higher magnitude, black carbon particles are noticeable. Figure 21b shows a TEM image of the junction between an agglomerate and the elastomer matrix. On the ellipsoidal elements, particle concentration density of black carbon is far more important which confirms aggregation. Particle diameters in the range of 20–25 µm are also in correlation with high reinforced fillers used in the formulation. On the other hand, the material also contains some impurities of another type of carbon black, as shown in Figure 22. Their diameter particles are bigger.

To establish the state of black carbon dispersion, a statistical analysis was conducted by measuring the surface area of the frames and agglomerates. For comparison purposes, the analyzed surface area of each batch is nearly the same. Results are displayed in Table 5.

For each batch, the graph in Figure 23a illustrates the proportion represented by the agglomerates. Surprisingly, the lowest proportion is found in the batch with the lowest SpinTest performance ($\eta_{lot\ A} = 1.51\%$). In comparison, batches B and C, which have better performance on valves, have slightly higher proportions ($\eta_{lot\ B} = 2.56\%$;

Table 5. TEM analysis results.

Batch	Performance index (SpinTest)	Frames number analyzed ($S_{\mathbf{frames}}$)	Black agglomerates found	Surface area of black carbon agglomerates ($S_{agglomerates}$)	Percentage surface area of agglomerates $\eta = S_{agglomerats/S\_cframes}$	Frame number without agglomerates (S_{void})	$\lambda = (S_{void})/$ SFrames	Average surface area of the agglomerates (μm^2)
A	0.26	122 (3.79 mm^2)	132	0.058 mm^2	1.51%	45 (1.11 mm^2)	29.3%	452 μm^2 (σ = 1151 μm^2)
B	0.59	128 (3.65 mm^2)	142	0.093 mm^2	2.56%	52 (1.35 mm^2)	37%	658 μm^2 (σ = 591 μm^2)
C	0.84	114 (3.46 mm^2)	94	0.061 mm^2	1.76%	44 (1.28 mm^2)	37%	626 μm^2 (σ = 486 μm^2)

$\eta_{lot\ C} = 1.76\%$). Thus, there seems to have no relation between the agglomerates surface quantity and the SpinTest performance and the lifetimes of the specimens. Referring to the average sizes of the agglomerates (last column of Tab 5.), once again, lot A has the best dispersion despite low I_{perf}, followed by batches C and B. However, a significant deviation of results is observed in batch A compared to others. Among the 132 identified agglomerates, the majority are small, but some are massive as shown in Figure 23b. The contribution of the five largest agglomerates in batch A accounts for approximately 45.6% of the total surface area of the agglomerates, compared to 16.4% and 18.9% for the other batches. Therefore, the statistical analysis reveals a significant standard deviation.

By relating these data to the dynamic performance, a trend emerges (Fig 24a), failures appear to be primarily governed by the presence of agglomerates of significant sizes. Good performance in SpinTest or in fatigue on rubber specimens is achieved when the reduction of the secondary structure of carbon black is maximal, limiting the presence of large agglomerates.

Excluding the batch A, which has large agglomerates that result in poor fatigue performance, the batch C, with excellent performance, stands out from batch B. The number of agglomerates identified is lower, and their size and standard deviation are smaller. As a result, the dispersion of carbon black is more complete, indicating a more dispersing mechanism during mixing process. The emerging trend thus shows that better dispersion of the filler promotes good performance in fatigue, while the presence of large agglomerates within the matrix leads to mediocre dynamical performance. To support our argument, tomographic analyses of valves have also revealed the presence of carbon black agglomerates on the fracture surfaces. Figure 24b shows a carbon black agglomerate that is split into two distinct parts by a fissure. This clearly demonstrates the fragility of these heterogeneities.

5 Conclusion

Currently, rubber valves are suitable for passenger vehicles and pose no risks concerning the driver's safety. However, for high-speed applications, rubber valves are exposed to a risk of failure. A crack is likely to initiate, leading to a loss of sealing. In this context, to understand the causes of failures, rubber automotive valves were studied. Initially, a thorough understanding of the valve damage phenomena in high-speed application was established. The rubber crack initiation is localized in the sealing area of the valve, and the cracking results from repeated accelerations and decelerations of the wheel, causing significant cyclic centrifugal forces on the rubber. Although necessary for safety, it appears that the pressure sensor (TPMS) screwed onto the back of the valve significantly amplifies these forces. Since the center of gravity is located outside the wheel, at high rotational speeds, the valve and its sensor become unbalanced (lift down) and generate a concentration of mechanical stresses on the rubber in contact with the outer chamfer of the rim hole. Once the crack is initiated, it propagates within the component until rupture and loss of sealing occur. The intrinsic variability of the material was characterized through an experimental fatigue campaign on test specimens to eliminate the dominant variability factor related to the testing equipment. A numerical approach based on the invariants of the Hencky strain tensor was used. These invariants were first used to establish a characteristic deformation state of the crack initiation zone on valves and then transposed onto a customized fatigue specimen to approach a loading condition representative of the real application of a rotating wheel at 1050g. For this purpose, considering the elastomer nearly incompressible, two invariants were utilized, one quantifying the deformation intensity (K_2) and the other indicating the mode of loading (K_3). After experimentation, it was found that the theoretical deformation intensity obtained from K_2 was not suitable for the chosen mechanical profile to characterize the durability of the specimens (time criterion). Therefore, it was decided to characterize the variability of the specimen lifetimes at various deformation amplitudes. The result, illustrated by a Wöhler representation, confirms with respect to the initial problem that material exhibits significant intra and inter batch variability. Fatigue test results show that the conducted tests are experimentally representative of the valve's performance. The batch with a long SpinTest lifespan exhibits good durability on the test specimens, while the batches with short lifespans show the opposite. The chosen failure criterion, based on the drop in the elastic modulus, has revealed that premature failures occur regardless of the deformation amplitudes experienced by the material, even for a batch with good SpinTest performance. Fractographic analyses performed on these specimens reveal high concentrations of carbon black on the surface, originating from poorly dispersed agglomerates. These significant inhomogeneities, identified through tomography and TEM, act as stress concentrators in the elastomer matrix and generate weaknesses under fatigue loading. These weaknesses can lead to crack initiation and promote their propagation in the test specimens.

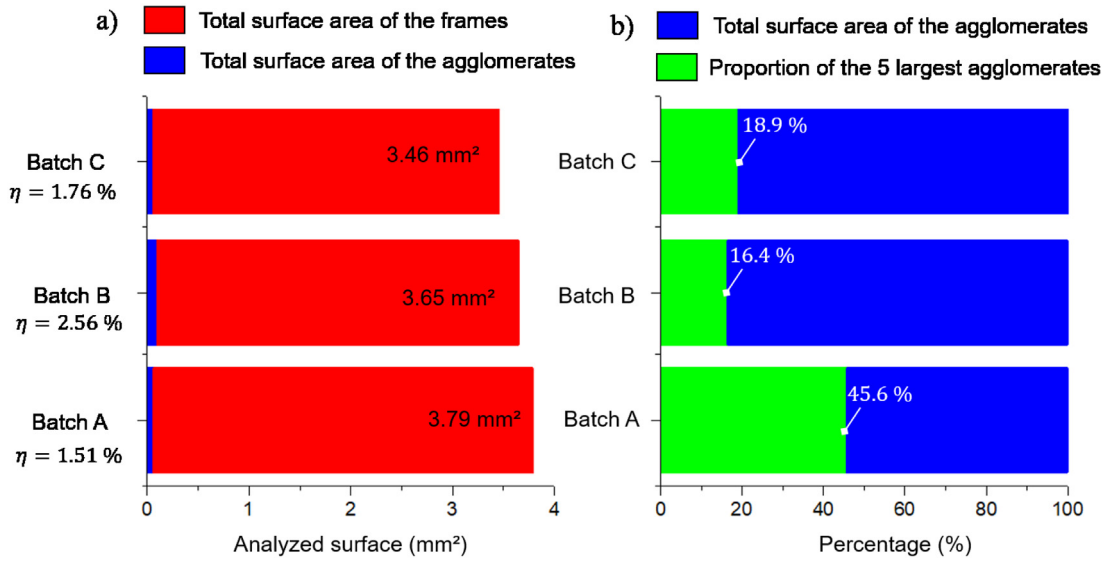

Fig. 23. (a) Demonstration of the surface area proportion of the agglomerates in the entire set of samples; (b) contribution of the five largest agglomerates. The percentage η corresponds to the surface area percentage of the agglomerates compared to the frames.

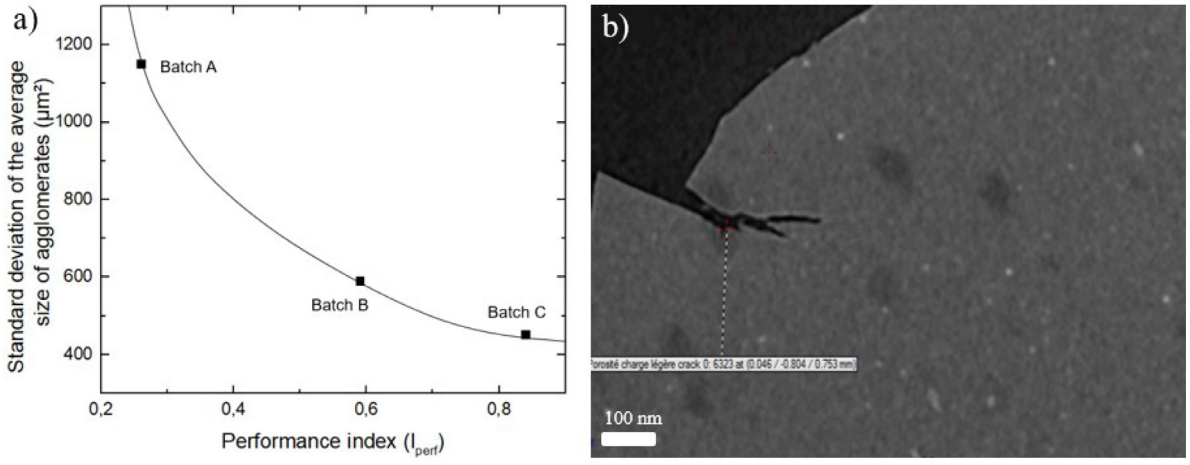

Fig. 24. (a) Standard deviation of agglomerate sizes versus SpinTest performance; (b) crack sectioning a carbon black agglomerate.

Fractography also reveals the presence of impurities in the material, which can contribute to mechanical fragility. Furthermore, the carbon concentrations are covered on the surface by a layer of tongues. These morphologies allow us to affirm that a fatigue wear phenomenon occurs in the rubber related to the agglomerates in these areas. Finally, the TEM analyses reveal and confirm that the key to achieving good dynamic performance lies in the quality of filler dispersion. One of the main factors of failure is directly related to large agglomerate sizes. Since the mixture is heavily loaded with a very fine black substance, charge-to-charge interactions in the mixer are significant, requiring careful mixing to ensure proper ingredient dispersion. To better control the variability of mechanical properties, it is crucial, first of all, to limit contaminants that may arise during the rubber manufacturing process. Cleaning blends can be implemented between two productions of different masterbatches to prevent cross-contamination of ingredients. Maintaining a high level of cleanliness is also essential to avoid volatile contaminants within the factory. Regarding the dispersion of carbon black fillers, it can be enhanced by optimizing mixer parameters such as rotor speed and temperature while favoring longer mixing times. It is possible to pre-treat the carbon black to reduce its secondary structure, facilitating its dispersion in the matrix. Dispersing agents can also be employed to improve the affinity of carbon black with the polymer matrix, promoting a more homogeneous dispersion.

Acknowledgment

Special thanks to Angius Alain, Giles Capdepon (Continental Automotive Toulouse) and Manero Florence (SCIAM : Service Commun d'Imageries et d'Analyses Microscopiques de l'Université de Angers).

Funding

This research was funded by Continental Automotive Toulouse during my PhD work. The APC was funded by Université de Tours, France.

Conflict of interest

RF has received funding from Continental Automotive. The authors MP, FL, FC, SC, MV, MS have nothing to disclose.

Data available statement

Data associated with this article cannot be disclosed due to professionnal confidentiality from the company.

Author contribution statement

Conceptualization, Stéphane Couarraze; Methodology, Rodolphe Forasacco, Florian Lacroix, Stéphane Méo and Marie-Pierre Deffarges; Software, Stéphane Méo and Florent Chalon; Validation, Rodolphe Forasacco, Stéphane Couarraze,and Florian Lacroix; Formal Analysis, Rodolphe Forasacco; Investigation, Rodolphe Forasacco; Resources, Stéphane Couarraze; Data Curation, Rodolphe Forasacco; Writing – Original Draft Preparation, Rodolphe Forasacco; Writing – Review & Editing, Rodolphe Forasacco, Florian Lacroix, Stéphane Méo, Marie-Pierre Deffarges and Stéphane Couarraze; Visualization, Rodolphe Forasacco; Supervision, Stéphane Couarraze and Florian Lacroix; Project Administration, Stéphane Couarraze; Funding Acquisition, Stéphane Couarraze.

References

[1] J.C. Criscione, J.D. Humphrey, A.S. Douglas, W.C. Hunter, An invariant basis for natural strain which yields orthogonal stress response terms in isotropic hyperelasticity, J. Mech. Phys. Solids **48**, 2445–2465 (2000)

[2] International Carbon Black Association (ICAB), Carbon black user's guide, safety, health, & environmental information (2004)

[3] Y. Fan, G.D. Fowler, M. Zhao, The past, present and future of carbon black as a rubber reinforcing filler: a review, J. Clean. Prod. **247** (2020)

[4] A.M. Gessler, Effect of mechanical shear on the structure of carbon black in reinforced elastomers, Rubber Chem. Technol. **43**, 943–959 (1970)

[5] M. Klüppel, The role of disorder in filler reinforcement of elastomers on various length scales, Adv. Polym. Sci. **164**, (2003). DOI:10.1007/b11054

[6] ASTM.D.1765-99. Standard classification system for carbon blacks used in rubber products, SUPERSEDED, 1999B EDITION, May 10, 1999

[7] N. Saintier, G. Cailletaud, R. Piques. Cyclic loadings and crystallization of natural rubber: an explanation of fatigue crack propagation reinforcement under a positive loading ratio, Mater. Sci Eng. A **528**, 1078–1086 (2011)

[8] I. Masquelier, Influence de la formulation sur les propriétés en fatigue d'élastomères industriels. Thèse de Doctorat, Université de Bretagne Occidentale (2014)

[9] J. Grandcoin, A. Boukamel, S. Lejeunes, A micro-mechanically based continuum damage model for fatigue life prediction of filled rubbers, Int. J. Solids Struct. **51**, 1274–1286 (2014)

[10] S.V. Hainsworth, An environmental scanning electron microscopy investigation of fatigue crack initiation and propagation in elastomers, Polym. Test. **26**, 60–70 (2007)

[11] J.-L. Poisson, F. Lacroix, S. Meo, G. Berton, N. Ranganathan, Biaxial fatigue behavior of a polychloroprene rubber, Int. J. Fatigue **33**, 1151–1157 (2011)

[12] J.-B. Le Cam, B. Huneau, E. Verron, L. Gornet, Mechanism of fatigue crack growth in carbon black filled natural rubber, Macromolecules **37**, 5011–5017 (2004)

[13] G. Weng, H. Yao, A. Chang, K. Fu, Y. Liu, Z. Chen, Crack growth mechanism of natural rubber under fatigue loading studied by a real-time crack tip morphology monitoring method, RSC Adv. **4**, 43942–43950 (2004)

[14] G. Ayoub, M. Naït-Abdelaziz, F. Zaïri, Multiaxial fatigue life predictors for rubbers: application of recent developments to a carbon-filled SBR, Int. J. Fatigue **66**, 168–176 (2014)

[15] K. Legorjujago, Fatigue initiation and propagation in natural and synthetic rubbers, Int. J. Fatigue **24**, 85–92 (2002)

Cite this article as: R. Forasacco, M.-P. Deffarges, F. Lacroix, F. Chalon, S. Couarraze, M. Venin, S. Méo, Characterization and understanding of mechanical variability of elastomer: application in automotive valve testing in low cycles fatigue, Mechanics & Industry 25, 14 (2024)